

Multiaxial fatigue design of cast parts: Influence of complex defect on cast AS7G06-T6

P. Mu ^a, Y. Nadot ^{a,*}, I. Serrano-Munoz ^b, A. Chabod ^c

^a ISAE-ENSMA – UPR CNRS 3346, Institut Pprime, Département Physique et Mécanique des Matériaux, Téléport 2, Avenue Clément Ader, BP 40 109, 86961 Futuroscope, France

^b MATEIS, INSA Lyon/Université de Lyon/CNRS, F-69621 Villeurbanne Cedex, France

^c CTIF, 44 avenue de la Division Leclerc, F-92318 Sevres Cedex, France

AS7G06-T6 cast aluminum alloy is tested under tension, torsion and tension–torsion fatigue loading for two load ratios. Basquin's law and step loading method are used to obtain the fatigue limit under multiaxial loading. Crossland criterion and principal stress criterion considering Goodman idea are compared to evaluate the multiaxial behavior. The influence of complex defects on fatigue limit is analyzed under multiaxial loadings. Several artificial defects are machined on fatigue specimen with different distance between edges. A new definition of the equivalent defect size considering the distance between defect edges is proposed. For both tension and tension–torsion fatigue, the competition between single natural defect and complex artificial defects is observed and analyzed.

1. Introduction

The fatigue behavior under multiaxial loadings is an important issue in fatigue design of engineering components such as aircraft and automobile. However, the cyclic stress–strain responses under multiaxial loadings are very hard to analyze due to the complex loading path, which lead to the complexity in fatigue behavior description. Many criteria suitable to different loading conditions and materials have been proposed until now. They can be distinguished into three categories: criteria based on stress, strain and energy. A complete review of multiaxial fatigue criteria can be found in Ref. [1]. The first objective of this paper is to find an appropriate criterion that can be used for AS7G06-T6 under multiaxial fatigue loading. In this study, two well-known criteria in multiaxial fatigue domain are presented and applied in the analysis of experimental results under tension, torsion and tension–torsion loadings. The first criterion is the widely-used Crossland criterion [2]. The second one is based on the famous principal stress criterion, but considering Goodman idea in order to describe the influence of mean stress.

Many approaches have been proposed in order to assess the influence of a defect on the fatigue life. An overview of that problem can be found in Ref. [3]. The influence of a defect on fatigue life can be determined by 4 parameters:

- Defect type (inclusion, pore, shrinkage, oxide...).
- Defect morphology (spherical, elliptical, complex...).
- Defect position (internal, sub surface or surface).
- Defect size (function, or not, of loading direction).

* Corresponding author. Tel.: +33 5 49 49 80 43; fax: +33 5 49 49 82 38.
E-mail address: yves.nadot@ensma.fr (Y. Nadot).

Nomenclature

d_{edge}	distance between defect edges (μm)
f_i	area percentage of grains within a certain grain size zone
t, t_i, t_j	time (s)
E	Young's modulus (GPa)
$J_{1,max}$	maximum value of the first invariant of the stress tensor (MPa)
$J_{2,a}$	amplitude of the second invariant of the deviatoric stress tensor over a loading cycle (MPa^2)
R	load ratio between minimum and maximum stresses of the loading cycle
R_m	tensile strength (MPa)
$R_{p0.2}$	yield strength at 0.2% plastic deformation (MPa)
T	loading period (s)
α	material parameter in Crossland criterion
α_1	parameter in principal stress criterion considering Goodman idea
β_1	parameter in principal stress criterion considering Goodman idea (MPa)
ν	Poisson's ratio
$\Delta\sigma$	variation of stress amplitude between two steps in the "step loading" procedure (MPa)
$\sigma_1, \sigma_2, \sigma_3$	components in the principal coordinate system (MPa)
σ_a	stress amplitude in tension (MPa)
$\sigma_{a,I}, \sigma_{a,II}, \sigma_{a,III}$	components in the principal coordinate system corresponding to the stress amplitude tensor (MPa)
$\sigma_{a,ij} (i = 1, 2, 3)$	component of stress amplitude (MPa)
σ_{cr}	Crossland stress (MPa)
σ_D	fatigue limit corresponding to 5×10^6 cycles (or 2×10^6 cycles for tension–torsion loadings with artificial defects) (MPa)
$\sigma_{D-1,a}$	fatigue limit in tension with the load ratio $R = -1$ (MPa)
σ_{D0}	previous stress amplitude at which the specimen passed 5×10^6 cycles (MPa)
$\sigma_{D0.1,a}$	fatigue limit in tension with the load ratio $R = 0.1$ (MPa)
$\sigma_{D0.1,m}$	mean stress in tension corresponding to the fatigue limit in tension with the load ratio $R = 0.1$ (MPa)
$\sigma_{eq,cal}$	calculated equivalent stress (MPa)
$\sigma_{eq,exp}$	experimental equivalent stress (MPa)
$\sigma_{ij} (i = 1, 2, 3)$	stress component (MPa)
$\sigma_{m,ij} (i = 1, 2, 3)$	component of mean stress (MPa)
$\sigma_{m,I}, \sigma_{m,II}, \sigma_{m,III}$	components in the principal coordinate system corresponding to the mean stress tensor (MPa)
$\sigma_{m,pr}$	principal stress calculated with the mean stress tensor (MPa)
σ_{max}	maximum stress (MPa)
σ_{pr}	principal stress calculated with the stress amplitude tensor (MPa)
$\sigma_{pr,ghm}$	principal stress considering Goodman idea (MPa)
τ_a	stress amplitude in torsion (MPa)
$\tau_{D-1,a}$	fatigue limit in torsion with the load ratio $R = -1$ (MPa)
$\tau_{D0.1,a}$	fatigue limit in torsion with the load ratio $R = 0.1$ (MPa)
$\tau_{D0.1,m}$	mean stress in torsion corresponding to the fatigue limit in torsion with the load ratio $R = 0.1$ (MPa)
Φ	grain size (μm)
$\Phi_{def.}$	defect size (μm)
Φ_i	average grain size of grains within a certain grain size zone (μm)
$\bar{\sigma}_{pr}$	principal stress tensor
\bar{S}	deviatoric stress tensor
\sqrt{area}	characteristic length describing the defect size, projection of the defect surface on a plane perpendicular to the direction of the maximum principal stress (μm)

The fatigue design of a metallic cast part is strongly linked to the casting process. The designer needs to compromise between the fatigue resistance of the component and the allowable defect size due to the process. In order to perform this optimization, a criterion that takes into account for defect influence on the fatigue limit is necessary. Murakami [4] proposed an empirical approach where the defect is measured in relation with loading direction with the so called 'area' defect parameter. This approach can be applied for different defect morphologies and gives interesting results for steels. However, for complex defects, the equivalent defect size cannot always be measured directly. For example, for several defects located with a ligament between one another, one must decide whether the ligament should be considered into the calculation of the defect size. Some codes such as BS 7910 [5], R6/4 [6] and ASME Section XI [7], provide procedures to re-characterize neighboring defects with interactions, or defects with complex shapes into simpler defects with idealized shapes. These re-characterized defects must be proven to be more noxious than the original ones to ensure the conservatism of the procedures. Experimental studies [8–11] have demonstrated limited crack interaction effects under bending as the adjacent crack tips

approach, and numerical analyses [11–14] show enhanced values of stress intensity factors for very closely spaced crack tips. Recent revisions of BS 7910 and R6/4 incorporate limited interaction effects in fatigue but preclude the contribution of coalescence to the fatigue life, by re-characterizing interacting defects when the adjacent crack tips touch. The second objective of this paper is to analyze the influence of complex defects in uniaxial tension and biaxial tension–torsion and create a new criterion to consider this influence.

The following points are addressed in this paper. First, fatigue tension, torsion and tension–torsion tests were performed on specimens with and without defects and the fatigue limits under different loading conditions were identified. Second, the identification and error analysis were done for two multiaxial criteria: Crossland criterion and principal stress criterion considering Goodman idea. Third, the influence of natural (shrinkage cavity), single and complex (3 defects under tension and 9 defects under tension–torsion) artificial defects on fatigue limit were analyzed and compared to that of defect-free specimens. A criterion was proposed to calculate the equivalent defect size for complex defects under fatigue tension. The competition between a single natural defect and complex artificial defects under uniaxial and multiaxial fatigue loadings was observed and the explained using Kitagawa diagram.

2. Material

The material is a cast aluminum alloy AS7G06-T6. Its chemical composition is given in Table 1. The material was supplied as cast as a bar of 270 mm length and 30 mm diameter. Two cylindrical specimens were machined off the bar. All specimens (tension, torsion and tension–torsion) have the same gage section: useful length of 20 mm and diameter of 10 mm. As for the casting procedure, the cast aluminum alloy AS7G06 T6 obtained by gravity die casting. 95 kg 100% new ingots were casted in each casting, which correspond to 40 specimens. An electric furnace was used. The casting temperature was 720 ± 10 °C and the mold temperature is 350 °C when closing die. Opening and shake-out lasted 120 s after filling. Hydrogen degassing and oxide removing were done by argon injection into aluminum bath (5–7 l/min during 7 min, before and after composition corrections) with 0.1% deoxidation flux COVERAL GR 2410 and a 0.05% degassing flux. Besides composition, the temperature, porosity rate and density were also controlled during casting. The thermal treatments in the T6 condition are: heating to solution at 540 °C for 10 h, quenching in cold water, waiting 24 h at room temperature, then returning to 160 °C for 8 h.

Electron Backscatter Diffraction (EBSD) measurements were performed on the specimen surface. EBSD scans were performed in beam control mode with a spatial resolution of 5 $\mu\text{m}/\text{step}$. The zone (6.0×5.0 mm²) scanned in SEM contains 1449 grains. As shown in Fig. 1a, the grain size (diameter Φ of a disk having the same area as the grain) of the material varies from 28 to 1305 μm . Its average grain size is 259 μm , with a standard deviation of 215 μm . The distribution of grain area percentage for different grain sizes is also shown. The total area of the grains within each grain size zone is cumulated and divided by the total grain area in the observation zone. It can be seen that the grains between 500 and 600 μm occupy 17.4% of the total area, and the grains in the zone $\Phi \in [300, 800 \mu\text{m}]$ occupy about 3/4 of the total grain area. The average grain size considering the grain size percentage can be calculated below:

$$\Phi_{avg} = \sum_i \Phi_i \cdot f_i \quad (1)$$

where Φ_i is the average grain size of grains within a certain grain size zone and f_i is the area percentage of grains within a certain grain size zone. The average grain size considering grain area percentage is 573 μm . The grain size may play an important role in fatigue mechanisms. This is maybe because the grain boundaries act as natural barriers of crack propagation and thus required an additional energy to propagate the crack in the next grain [15,16].

The observation by optical microscope reveals the microstructure of the material at a smaller scale. A dendritic structure is observed (solid solution primary α and eutectic Al–Si surrounding), as seen in Fig. 1b. Shrinkage cavities could also be seen in Fig. 1b. The measurement the Secondary Dendrite Arm Spacing (SDAS) was done by dividing the distance of several secondary dendrite arms by the number of arms. Only the dendrites with at least 6 arms have been used in the measurement in order to reduce the measurement error. 155 dendrites were measured. The SDAS varies between 26 and 57 μm , following a normal distribution. 3/4 of the SDASes are located in the zone [31, 43 μm]. The average SDAS is 38 μm , with a standard deviation of 6 μm .

3. Experimental results

3.1. Specimens and experimental procedures

The specimens were observed by Non Destructive Testing (NDT): X-ray (XR) and Die Penetrant Liquid. The numerical X-ray detection has been done using the specification NF EN 12681 and the equipment Tube Yxlon Y.TU/320-D03. The

Table 1
Composition of the AS7G06-T6 (wt.%).

Si	Mg	Fe	Cu	Mn	Ni	Zn	Pb	Sn	Ti
7.00	0.56	0.097	<0.015	<0.03	<0.01	<0.01	<0.003	<0.01	0.13

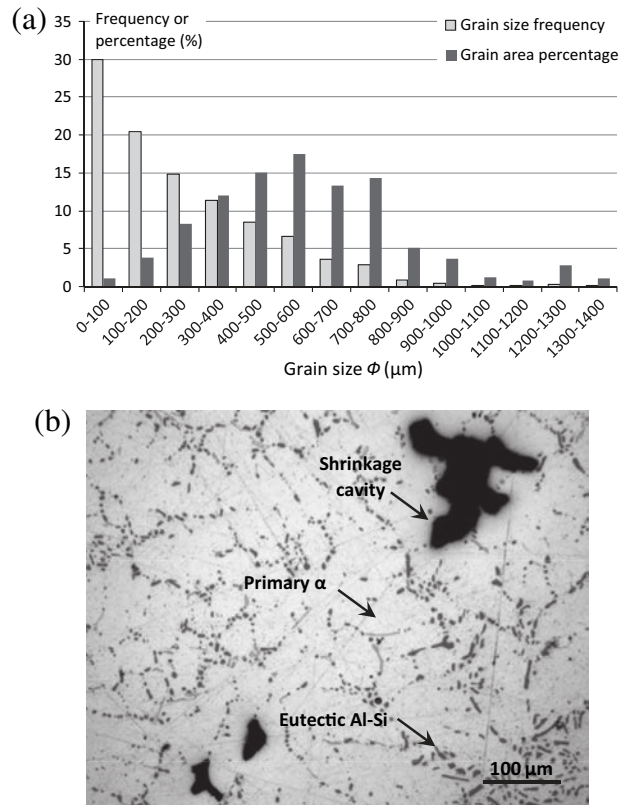


Fig. 1. (a) Distributions of grain size frequency (1449 grains) and of grain area percentage and (b) microstructure of AS7G06-T6.

detecting thickness was 30 mm. The voltage was 90 kV. The focus-to-film distance was 1 m; the geometric unsharpness was 0.15 mm; and the angle of incidence was 90°. The specimen was exposed for 30 s in the intensity 5. The visible Image Quality Indicator (IQI) was W12 (0.25 m) following the specification NF EN 462-1. The Die Penetrant Liquid detection was done following specifications NF EN 571-1 and NF EN 1371-1. Visible lighting was used, with residual under UV of 6 lux and under ultraviolet of 14 W/m². A fluorescent penetrant of sensibility S2 was adopted. The impregnation time was 20 min and the temperature was 22 °C. The penetrant was later eliminated with water and air, under a pression below 2 bars. After a drying procedure under 45 °C for 3 min, a dry revelator was applied. After 10 min, the specimen was ready for examination. The recording time was controlled to be under 30 min.

7 Specimens have been used to analyze the size distribution and the porosity ratio of shrinkage cavities. The plug-in Fiji "Labeling 3D" was adopted to identify the size of each cavity in the stack, whereas the plug-in "fracz" which ran through each slice of a stack (there are 2,400 slices per stack) was used to analyze the volume fraction of shrinkage cavities. 1,372 shrinkage cavities were detected. Over 88% of the analyzed pores have a volume between 20,000 and 60,000 μm^3 . As for the porosity ratio, 16,800 slices in 7 stacks were analyzed. The pore ratio in terms of volume fraction is 0.00181%.

Sample tested are classified as grade 1 according to ASTM E155 [17], Al alloys, shrinkage cavity, 1/4 inch. Samples have therefore a minimum amount of shrinkage. Die Penetrant can reveal some oxides at the free surface. All samples containing oxides were rejected for fatigue tests, as done for the industrial components. Uniaxial tensile tests were done following the specification NF EN ISO 6892-1 on a machine ZWICK BT1.FR100THW.A2K, whose capacity is 100 kN. 3 cylindrical specimens with a diameter of 10 mm and a useful length of 50 mm, were tested. The extensometer ZWICK BTC-EXMACRO.011 has a basic length of 50 mm. The deformation rate was 0.00007 s⁻¹ for the measurement of $R_{p0.2}$, and 0.002 s⁻¹ for R_m . The material has a yield strength $R_{p0.2} = 275$ MPa and a tensile strength $R_m = 335$ MPa. The average value of Young's modulus E over three specimens is 73 GPa and the Poisson's ratio ν is 0.3.

In order to get the fatigue limits of AS7G06-T6 under multiaxial loadings, tension, torsion and tension-torsion fatigue tests have been performed. Tension fatigue tests were performed by the means of Amsler vibrophore (electromagnetic resonance machine) under force control. The test frequency was 108 Hz. The drop of test frequency (5 Hz) was adopted as the stop condition of fatigue tests. When a test is stopped under this condition, the sample is almost broken and contains a macroscopic crack deeper than half diameter of the sample. Fatigue tests were conducted at two load ratios: $R = -1$ and 0.1. Tension and tension-torsion tests with the load ratio $R = 0.1$ were conducted on a servo-hydraulic fatigue testing machine - Instron 1343. This machine model enables both static and fatigue tests with a dynamic capacity up to

±250 kN. The tension–torsion tests have been made with the same stress amplitudes under traction and torsion. Torsion tests with the load ratio $R = -1$ were performed on a MTS servo-hydraulic machine of the model 809 with axial/torsional test system, whose maximum force capacity was 100 kN. The test frequency was 10 Hz. The tests were conducted under control of maximum stress. For all tension, torsion and tension–torsion tests, the loadings were sinusoidal. Fatigue limits are given using the amplitude defined as the maximum stress minus the mean stress over the load cycle.

In order to be able to produce Kitagawa type diagrams [18] for different defect sizes and different types of defect, the “step loading” procedure was used to evaluate the fatigue limit on one sample [19]. The fatigue test was started on a sample at a given load for 5×10^6 cycles (or 2×10^6 cycles for most tension–torsion tests with artificial defects in order to reduce the testing time). If the sample was broken at the initial stress amplitude, the endurance limit was lower than the applied stress amplitude. Of course this is a deterministic view of the result that does not take into account the scatter. It is therefore possible to have a sample failed below the average fatigue limit less than 5 (or 2) million cycles. In absence of any failure, it was considered that the corresponding endurance limit is higher than the recent stress amplitude and the sample was loaded again at a higher stress level. In this study the increase of stress amplitude was 10 MPa in tension tests. This procedure was repeated until failure. In this case, the endurance limit can be calculated as below:

$$\sigma_D = \sigma_{D0} + \frac{\Delta\sigma}{2} \quad (2)$$

where σ_{D0} is the previous stress amplitude that the specimen passed 5×10^6 (or 2×10^6) cycles, and $\Delta\sigma$ is the variation of stress amplitude between two steps ($\Delta\sigma = 10$ MPa here).

Bellows et al. [19] used the procedure on Ti64. It is the only procedure to evaluate the fatigue limit of a sample for a natural defect because it is impossible to generate an $S-N$ curve for a set of samples containing the same defect type, location and size. The analysis of the set of results will inform whether or not the material is sensitive to the famous coaxing effect [20]. In the AS7G06-T6 tested there is no evidence of the effect of loading history. It seems therefore that the step loading is appropriate to make an estimation of the fatigue limit using one sample.

3.2. Experimental results under multiaxial loadings

As presented in the literatures [21–24], the aluminum alloys have no evident fatigue limit. So we use the Basquin’s law to moderate the $S-N$ curves in Fig. 2. For the load ratio $R = -1$ (0.1), 15 (10) experimental points are used in the identification in tension tests, and 10 (4) points are used in torsion tests. Results obtained in Fig. 2 are supposed to be “defect free” in the sense of an industrial classification: class 1 ASTM E155 Al alloy, shrinkage cavity, 1/4 inch plus Die Penetrant surface examination. They will be used in the following as base for comparing multiaxial criteria and also as the reference “defect free” material on the Kitagawa diagram to study the influence of the defect. These results are in agreement with others on identical or very similar materials [23,25–28].

Fig. 2 shows the $S-N$ curves for the alloy AS7G06-T6 under tension and torsion for different load ratios $R = -1$ and 0.1. By using the Basquin’s law, the fatigue limits under the four loadings above for 5×10^6 cycles can be identified and listed in Table 2.

Fig. 3 shows the determination procedure of the fatigue limit in tension–torsion for a load ratio $R = 0.1$. Among the four tested specimens marked “defect free”, the specimen with no defect failed at 40 MPa. The other three specimens failed from shrinkage cavity. One of them failed at 50 MPa from a shrinkage cavity of 420 μm , the second and the third one failed at 40 MPa from a shrinkage cavity of 285 and 187 μm separately. It will be presented later that for these defect sizes, a natural or artificial defect has no influence on the fatigue limit for AS7G06-T6, so the experimental results from the four specimens with small shrinkage cavities or without defect can be used in the identification of the fatigue limit in tension–torsion. For

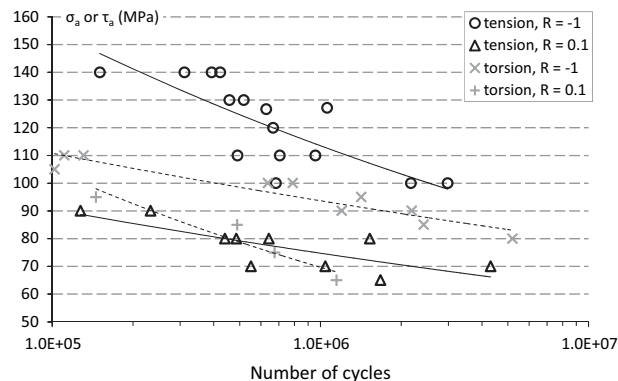
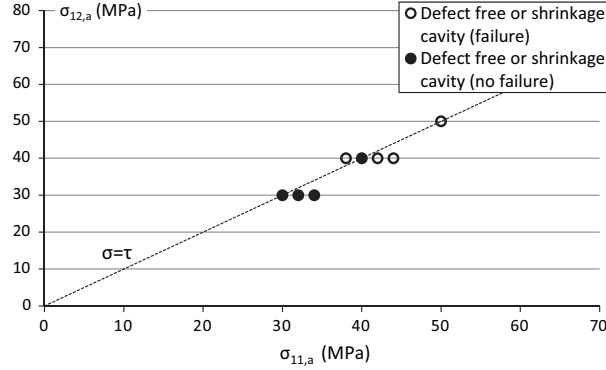


Fig. 2. $S-N$ curves for the alloy AS7G06-T6 under tension and torsion for different load ratios.

Table 2

Experimental fatigue limits under uniaxial and biaxial loadings.

No.	Type	R	$\sigma_{D-1,a}$ (MPa)	$\tau_{D-1,a}$ (MPa)	$\sigma_{D0.1,a}$ (MPa)	$\sigma_{D0.1,m}$ (MPa)	$\tau_{D0.1,a}$ (MPa)	$\tau_{D0.1,m}$ (MPa)
1	Tension	-1	90.9					
2	Tension	0.1			65.6	80.2		
3	Torsion	-1		80.0				
4	Torsion	0.1					68.7	84.0
5	Tension-torsion	0.1			37.5	45.8	37.5	45.8

**Fig. 3.** Identification of the fatigue limits in tension-torsion ($R = 0.1$) using the “step loading” method.

the specimen with no defect and failed directly at the first loading step, the fatigue limit can be identified using the Basquin's law. For the other three specimens, the fatigue limit is the mean stress amplitude of the last two loading steps. The mean value of the fatigue limit for “defect free” specimens is 37.5 MPa.

The fatigue limits of 5 different load types and two load ratios identified above are listed in Table 2. For load ratio $R = 0.1$, the mean stresses corresponding to fatigue limits are also given.

3.3. Fatigue criteria for AS7G06-T6

Crossland criterion [2] is first adopted and analyzed in this study for multiaxial loadings. The Crossland equivalent stress σ_{cr} is a linear combination of the amplitude of the second invariant of the deviatoric stress tensor $J_{2,a}$ and the maximum hydrostatic stress $J_{1,max}$.

$$\sigma_{cr} = \sqrt{J_{2,a}} + \alpha \cdot J_{1,max} \quad (3)$$

The calculation of $J_{2,a}$ is obtained by a double maximization over the loading period [29]:

$$J_{2,a} = \frac{1}{2\sqrt{2}} \max_{t_i \in T} \left\{ \max_{t_j \in T} \sqrt{(\bar{S}(t_i) - \bar{S}(t_j)) : (\bar{S}(t_i) - \bar{S}(t_j))} \right\} \quad (4)$$

$J_{1,max}$ is calculated as below:

$$J_{1,max} = \frac{1}{3} \max_{t \in T} \{ \sigma_{11}(t) + \sigma_{22}(t) + \sigma_{33}(t) \} \quad (5)$$

α can be identified in different ways. For example, it can be identified using the fatigue limits both in tension and torsion with the same load ratio $R = -1$ or 0.1 to focus on the behavior under multiaxial loadings. In this study, in order to consider the influence of load ratio, α was identified using the fatigue limits under tension with two load ratios $R = -1$ and 0.1: $\sigma_{D-1,a}$ and $\sigma_{D0.1,a}$. $\alpha = 0.801$, $\sigma_{cr} = 76.8$ MPa. The simplification form of the Crossland criterion and the identification of the parameter α can be found in Ref. [30].

Fig. 4 shows the $\sigma_{11,a} - \sigma_{12,a}$ curves simulated with Crossland with the fatigue limits under tension, torsion and torsion for different load ratios. As the identification of parameter α was done using $\sigma_{D-1,a}$ and $\sigma_{D0.1,a}$, the simulated curved passed these two experimental points. In torsion, the simulated σ_{cr} was slightly underestimated for the load ratio $R = -1$ and slightly overestimated for the load ratio $R = 0.1$. It is slightly larger than the experimental value under tension-torsion for the load ratio $R = 0.1$, too. More details will be given in the following error analysis.

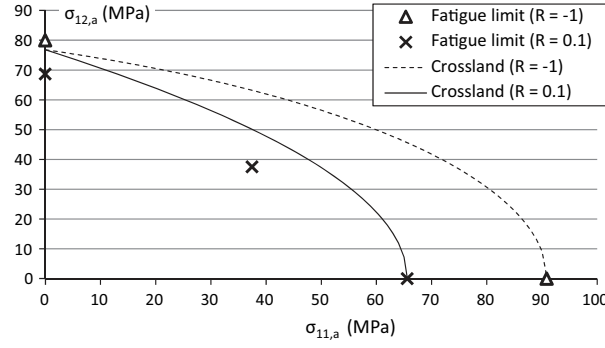


Fig. 4. Fatigue limits in tension ($R = -1$ and 0.1), torsion ($R = -1$ and 0.1) and tension-torsion ($R = 0.1$) with the simulated curve using the Crossland criterion ($R = -1$ and 0.1).

Table 3

Error analysis for Crossland criterion for 5 different load types presented in Table 2 (%).

Identification	No. (load type)				
	1 (tension)	2 (tension)	3 (torsion)	4 (torsion)	5 (tension-torsion)
$\sigma_{D-1,a}$ and $\sigma_{D0.1,a}$	0	0	4.00	-11.79	-17.07

Table 3 shows the error analysis for the Crossland criterion for 5 different load types presented in Table 2. The error is defined as below:

$$Error = \frac{\sigma_{eq,exp} - \sigma_{eq,cal}}{\sigma_{eq,exp}} \cdot 100\% \quad (6)$$

where $\sigma_{eq,exp}$ is the Crossland equivalent stress calculated with Eq. (3) for each load type with the fatigue limits identified experimentally. And $\sigma_{eq,cal}$ is the Crossland equivalent stress calculated using load type 1 or 2, which equals to 76.8 MPa. As the parameter α in the Crossland criterion was identified with $\sigma_{D-1,a}$ and $\sigma_{D0.1,a}$, the errors for specimens 1 and 2 were zero. It can be seen that the errors for torsion ($R = 0.1$) and tension-torsion ($R = 0.1$) are reasonable: -11.8% and -17.1% respectively. The average value of the absolute errors for 5 load types $|\overline{Error}|$ is 6.6%. This shows that Crossland criterion is relatively accurate to describe the multiaxial behavior of cast aluminum. However, as can be seen in this study, when the parameter in Crossland criterion is identified by the experimental results in tension, the criterion will give higher error in torsion. Moreover, the error for the load ratio $R = 0.1$ are higher than that for $R = -1$ in torsion, too. In order to simulate the behavior of AS7G06-T6 under multiaxial loadings and have a better consideration of the influence of mean stress, a new criterion based on the principal stress criterion will be compared to Crossland criterion.

The principal stresses are the components of the stress tensor when the basis is changed in such a way that the tensor is diagonal. The principal stress criterion with respect of the method of Goodman is based on the principal stress criterion. However, the new criterion considers also the influence of mean stress, as inspired by Goodman idea. As presented in Eq. (7), a stress tensor can be divided into two parts, one part of stress amplitude, and the second part of mean stress. These two parts are then used to calculate the corresponding principal stresses. They are considered to have a linear relation, and the experimental results in Table 2 can be used to identify the two parameters α_1 and β_1 in Eq. (7). The principal stress criterion with respect of the method of Goodman is then defined as in linear relation with the principal stress calculated using the mean stress, as seen in Eq. (7).

$$\left\{ \begin{array}{l}
 \bar{\sigma} = \begin{bmatrix} \sigma_{11} & \sigma_{12} & \sigma_{13} \\ \sigma_{12} & \sigma_{22} & \sigma_{23} \\ \sigma_{13} & \sigma_{23} & \sigma_{33} \end{bmatrix} = \begin{bmatrix} \sigma_{a,11} & \sigma_{a,12} & \sigma_{a,13} \\ \sigma_{a,12} & \sigma_{a,22} & \sigma_{a,23} \\ \sigma_{a,13} & \sigma_{a,23} & \sigma_{a,33} \end{bmatrix} + \begin{bmatrix} \sigma_{m,11} & \sigma_{m,12} & \sigma_{m,13} \\ \sigma_{m,12} & \sigma_{m,22} & \sigma_{m,23} \\ \sigma_{m,13} & \sigma_{m,23} & \sigma_{m,33} \end{bmatrix} \\
 \begin{bmatrix} \sigma_{a,11} & \sigma_{a,12} & \sigma_{a,13} \\ \sigma_{a,12} & \sigma_{a,22} & \sigma_{a,23} \\ \sigma_{a,13} & \sigma_{a,23} & \sigma_{a,33} \end{bmatrix} \rightarrow \begin{bmatrix} \sigma_{a,I} & 0 & 0 \\ 0 & \sigma_{a,II} & \\ 0 & 0 & \sigma_{a,III} \end{bmatrix} \rightarrow \sigma_{pr} = \max\{\sigma_{a,I}, \sigma_{a,II}, \sigma_{a,III}\} \\
 \begin{bmatrix} \sigma_{m,11} & \sigma_{m,12} & \sigma_{m,13} \\ \sigma_{m,12} & \sigma_{m,22} & \sigma_{m,23} \\ \sigma_{m,13} & \sigma_{m,23} & \sigma_{m,33} \end{bmatrix} \rightarrow \begin{bmatrix} \sigma_{m,I} & 0 & 0 \\ 0 & \sigma_{m,II} & \\ 0 & 0 & \sigma_{m,III} \end{bmatrix} \rightarrow \sigma_{m,pr} = \max\{\sigma_{m,I}, \sigma_{m,II}, \sigma_{m,III}\} \\
 \sigma_p = \alpha_1 \cdot \sigma_{m,pr} + \beta_1 \rightarrow \text{identification of } \alpha_1 \text{ and } \beta_1 \\
 \sigma_{pr, gdm} = \alpha_1 \cdot \sigma_{m,pr} + \beta_1
 \end{array} \right. \quad (7)$$

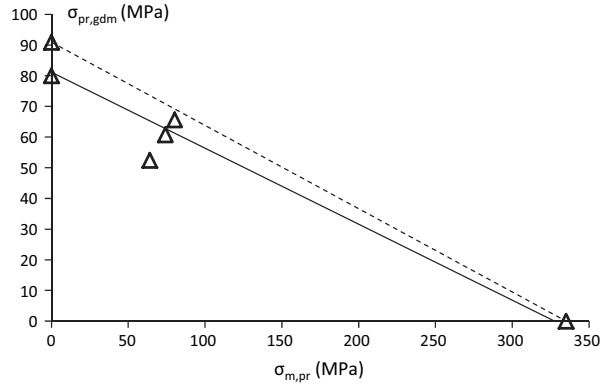


Fig. 5. Principal stress criterion considering Goodman idea for AS7G06-T6 with two methods of parameter identification (solid line: 5 fatigue limits listed in Table 2; dotted line: $\sigma_{D-1,a}$ and R_m).

Fig. 5 shows the identification of the parameters α_1 and β_1 using two experimental sources. The solid line was identified using 5 fatigue limits listed in Table 2, while the dotted line was identified using only $\sigma_{D-1,a}$ and R_m . The latter simpler identification method was analyzed in order to see whether it can be used to replace the first one. It can be seen from Fig. 5 that the two methods give similar parameters α_1 and β_1 . As tension–torsion tests were done only with the load ratio $R = 0.1$, there are no experimental results for $\sigma_{pr,gdm} < 50$ MPa. The error analysis for 5 load types using the new principal stress criterion is shown in Table 4. The new criterion gives large error for load type 4 for both two ways of parameter identifications. The error was calculated using Eq. (6), where $\sigma_{eq,exp}$ is the equivalent stress σ_{pr} calculated with Eq. (7) for each load type with the fatigue limits identified experimentally, and $\sigma_{eq,cal}$ equals to $\sigma_{pr,gdm}$ calculated with each $\sigma_{m,pr}$ in Eq. (7). With the parameters identified considering all 5 load types, both positive and negative errors can be seen. The average absolute error for 5 load types $|\overline{Error\ 1}|$ is 9.3%. If the parameters are identified using only $\sigma_{D-1,a}$ and R_m , the errors are either zero either negative. For load types 1, 2, 3 and 5, the absolute values of errors are below 20%. The average absolute error for 5 load types $|\overline{Error\ 2}|$ is 15.2%, which is much larger than $|\overline{Error\ 1}|$ and $|\overline{Error}|$. It seems that the new principal stress criterion considering Goodman idea is less accurate for the material.

In this section, Crossland criterion and principal stress criterion considering Goodman idea were tested for AS7G06-T6 under 5 load types. Although the parameter in Crossland criterion was identified using two fatigue limits in tension, this criterion can give reasonable results in tension, torsion and tension–torsion for two load ratios $R = -1$ and 0.1. The principal stress criterion without consideration of Goodman idea was also tested. However, this criterion seemed overestimated the influence of mean stress on fatigue under multiaxial loadings and gave an average absolute error over 20% for the 5 load types. So it is less accurate than Crossland's one for AS7G06-T6. The principal stress criterion considering Goodman idea corrected the influence of mean stress effectively. However, as it also gave much larger errors compared to Crossland criterion, it is not ideal for AS7G06-T6, either. Crossland criterion is thus adopted for the material under multiaxial loadings.

4. Influence of complex defects

4.1. Artificial defects and the influence of distance between defect edges

In order to estimate the influence of complex defects on fatigue limit under tension, 3 artificial defects were produced using the spark erosion machining. A copper wire carrying a current generates a high intensity electric arc that melts the material locally and machines desired defect. To obtain a spherical defect, the defect depth is equal to the diameter of the wire. In order to study the influence of the ligament, the defects were made on the surface of specimens with different distances between defect edges. Fig. 6a–c shows the photos from binocular microscope. With the same defect diameter and depth ($\approx 400\ \mu\text{m}$), the distance between defect edges d_{edge} varies between $650\ \mu\text{m}$ and 0. For $d_{edge} = 0$, three defects have become one big defect. The positions and shapes of defects can also be seen in Fig. 6d–f.

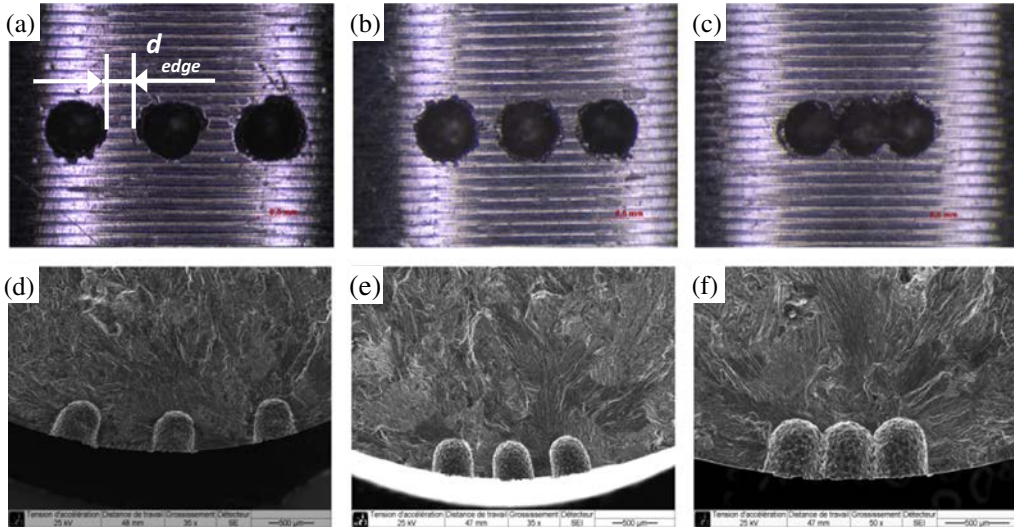
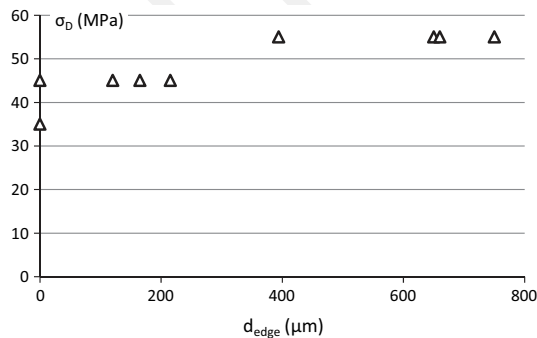
In this study, the parameter \sqrt{area} proposed by Murakami [4] was adopted to calculate the defect size for further analysis. \sqrt{area} is the projection of the surface of the defect on a plane perpendicular to the direction of the maximum principal stress. However, there is still no method to calculate \sqrt{area} for complex defects as in this study.

In order to identify the crack initiation sites, the fracture surface has been observed after failure, as seen in Fig. 6d–f. In this study, most cracks initiated from the three artificial defects. However, there was the competition between the artificial defects and natural defects (shrinkage cavities). This will be presented at the end of this study for discussion. The experimental results in this study are also compared to those in Refs. [30,31], in which the crack initiation site can be a crystallographic initiation without defect, a shrinkage cavity, an oxidized skin, or a single artificial defect. As in the previous work, the fracture surface for specimens with three artificial defects can also be divided into three parts: a crack initiation site where all the

Table 4

Error analysis for the principal stress criterion considering Goodman idea (%).

Identification	No. (load type)				
	1 (tension)	2 (tension)	3 (torsion)	4 (torsion)	5 (tension-torsion)
5 Fatigue limits listed in Table 2	10.77	6.68	-1.38	-24.49	-3.34
$\sigma_{D-1,a}$ and R_m	0	-5.40	-13.63	-40.34	-16.63

**Fig. 6.** Photos from binocular microscope (a–c) and fracture surface (d–f) of specimens with 3 defects with a different distance between defect edges. $\Phi_{def} = 400 \mu\text{m}$, $d_{edge} = 650 \mu\text{m}$ (a and d), $210 \mu\text{m}$ (b and e), 0 (c and f).**Fig. 7.** Influence of the distance between defect edges under tensile loading.

propagation rivers converge; a bright zone around the crack initiation site which corresponds to the stable fatigue crack propagation phase; a ductile zone far from the crack initiation site which corresponds to the final ductile fracture.

Fig. 7 shows the values of fatigue limit as a function of the distance between defect edges under tensile loading using the “step loading” method, see Eq. (2). It can be seen that for a defect size of $400 \mu\text{m}$, if the distance between the edges of two defects $d_{edge} > 400 \mu\text{m}$, there was no influence on the limit fatigue, the three defects can be regarded as isolated defects; if $d_{edge} < 200 \mu\text{m}$, the fatigue limit was reduced. This result shows that the ligament does have an influence on the fatigue limit, as long as d_{edge} is small enough ($d_{edge} < \text{defect size}$). So a method should be proposed to calculate the equivalent defect size.

4.2. Criterion for complex defects under uniaxial tension loading

For specimens with 3 surface defects, when d_{edge} is large enough, there will be no interaction between defects and they can be considered as isolated ones. On the contrary, when d_{edge} is smaller than a certain value ($\approx \sqrt{\text{area}}$ of one defect), the ligament between defects will be very thin and fragile so that the defect should be considered bigger and its size should be

calculated using the analytical method in Ref. [32], in which the size of the new big defect equals to the area of the polygon enclosing all 3 defects and the ligaments between them. By comparing the experimental results with those for one single defect in the Kitagawa diagram, the threshold value under which there will be the “ligament effect” was fixed equal to the defect size of a single defect, or 400 μm in this study. So the criterion to calculate the equivalent defect size for 3 defects can be expressed below:

If $d_{edge} < \sqrt{\overline{area}}$ of one defect, the 3 defects are considered as a big defect and the ligament can be considered in the calculation of the size of the big defect.

If $d_{edge} \geq \sqrt{\overline{area}}$ of one defect, the 3 defects are considered as 3 isolated defects.

Fig. 8 shows the Kitagawa diagram for 3 defects in comparison with the experimental results of single defects in Ref. [30]. The specimens with 3 defects of small d_{edge} had a large equivalent defect size and a lower fatigue limit compared to those with big d_{edge} , which is reasonable. The 5 specimens with a d_{edge} between 0 and 215 μm had an equivalent defect size between 725 and 812 μm and the σ_{max} was around 100 MPa. The 4 specimens with a d_{edge} larger than 400 μm had an equivalent defect size between 445 and 460 μm and σ_{max} was about 120 MPa. These results are in good agreement with those obtained in Ref. [30]. The method to calculate the equivalent defect size for complex defects has been proved correct for AS7G06-T6 under fatigue loading.

From Fig. 8 the fatigue limits for two big shrinkage cavities can be estimated. Their defect sizes are 508 and 755 μm and they both failed at σ_{max} between 89 and 111 MPa, which are in good agreement with the results of the artificial defects of the same sizes. So it can be concluded that using the parameter $\sqrt{\overline{area}}$ to characterize the defect size, a shrinkage cavity has similar influence on fatigue limit as a spark erosion machining defect of the same size.

4.3. Tension–torsion tests

In order to analyze the influence of complex defects on the fatigue behavior of AS7G06-T6 under biaxial loading, the specimens with 9 defects have been tested under tension–torsion loadings. The 9 defects have been made by spark erosion machining method with an identical defect size ($\sqrt{\overline{area}}$) of 400 μm . However, the distances between defect edges varied between 840 and 200 μm , as seen in Fig. 9.

Fig. 10 shows the Kitagawa diagram for tension–torsion tests. Tests were conducted with specimens with or without defects.

All tests were done under the same conditions. The stress amplitudes were the same both in tension and in torsion, with the load ratio $R = 0.1$. The “step loading” method was used to obtain the fatigue limit. The fatigue limit is the mean value of the stress amplitude at which the specimen failed in less than 2 million cycles and that of the stress amplitude of the last stress level at which the specimens underwent 2 million cycles.

4 Stress levels were applied in total. The experimental results have been slightly modified in the figure for the reason of presentation. For the specimens with one defect of 600 or 900 μm and 9 defects of 400 μm , the same results can be obtained. The fatigue limit was about 35 MPa. The specimens with a defect of 400 μm failed under the stress amplitude of 50 MPa, so $\sigma_D = 45$ MPa. This value is higher than that of the specimens with a defect of 600 or 900 μm and 400 μm 9 defects. According to the results above, we can see that there was no difference in the influence on the fatigue limit for a defect between 600 and 900 μm , but the fatigue limit was reduced compared to the result for a specimen with a defect of 400 μm . However, in order to confirm this conclusion, more specimens with defects of 400 μm should be tested. The fatigue limit for specimens with 9 defects of 400 μm is smaller compared to that of the specimens with a defect of 400 μm as well, but there was no

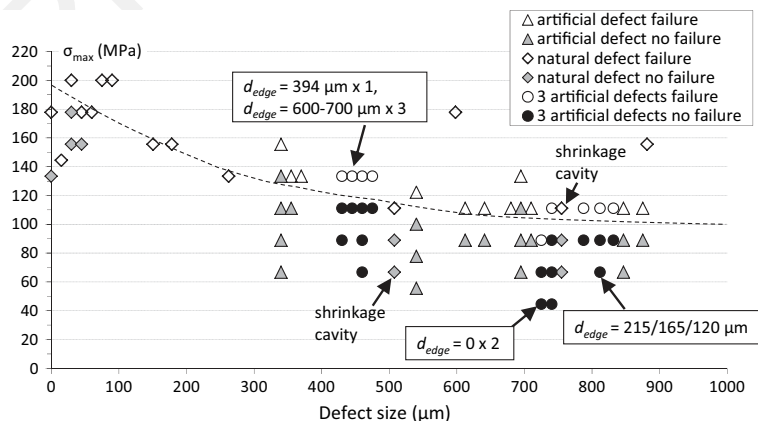


Fig. 8. Kitagawa diagram for the alloy AS7G06-T6 under uniaxial tension. Load ratio $R = 0.1$.

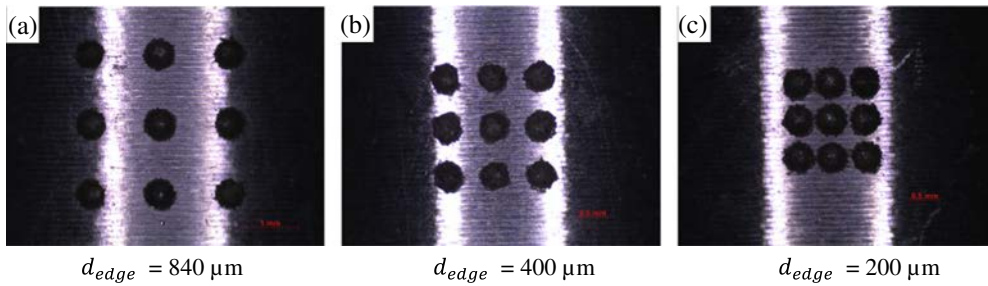


Fig. 9. Distribution of the 9 artificial surface defects with various distances between defect edges for tension–torsion tests.

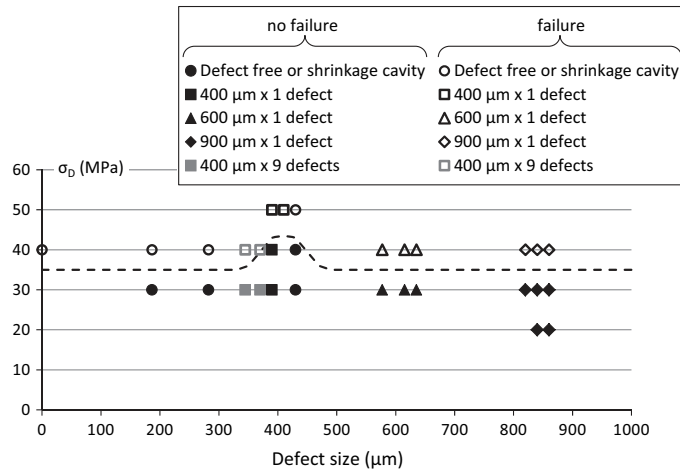


Fig. 10. Kitagawa diagram for the alloy AS7G06-T6 under tension–torsion. Load ratio $R = 0.1$.

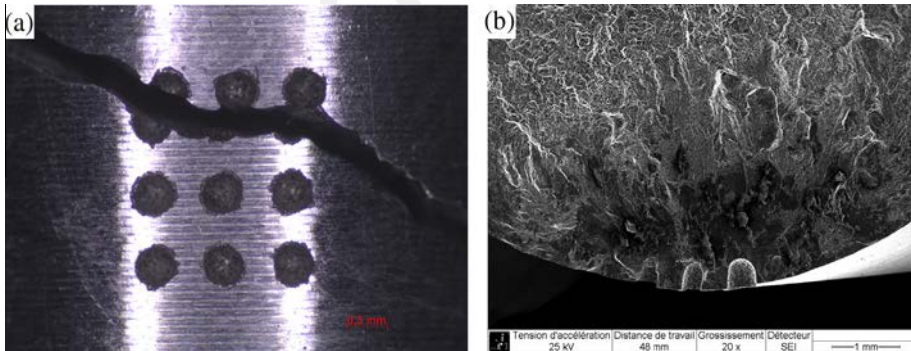


Fig. 11. (a) Specimen surface and (b) fracture surface of a tension–torsion specimen with 9 defects after failure.

difference among the three specimens with a different edge distance between defects. However, among the three specimens with 9 defects, the specimen with the smallest edge distance failed from a small surface shrinkage cavity of 187 μm . For the four tested specimens marked “Defect free or shrinkage cavity” in Fig. 10, three of them failed from a shrinkage cavity. One of them failed at 50 MPa from a shrinkage cavity of 430 μm . Two specimens failed at 40 MPa from a shrinkage cavity of 187 and 283 μm respectively. The last one which failed at 40 MPa had no defect. It can be concluded that σ_D is not influenced by defects smaller than 900 μm in tension–torsion tests ($\sigma_{a,11} = \sigma_{a,12}$), with a load ratio $R = 0.1$. Not like the case in tension tests, the influence of natural or artificial defect on fatigue limit of AS7G06-T6 is not obvious. Similar results can be found in the literature for A356-T6 [33,34].

For the two specimens with 9 artificial defects, the fracture surface passes by the three defects of the first row (see Fig. 11). For the 3rd specimen failed from one shrinkage cavity, the secondary crack passes by the defects of the first row, too.

Fig. 12 shows the fracture surface with initiation sites of a shrinkage cavity and of a defect-free specimen.

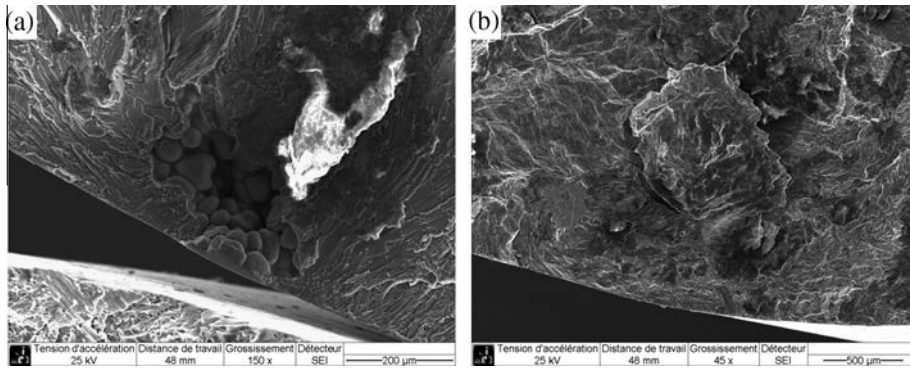


Fig. 12. Crack initiation under tension–torsion from (a) a shrinkage cavity or (b) without defect.

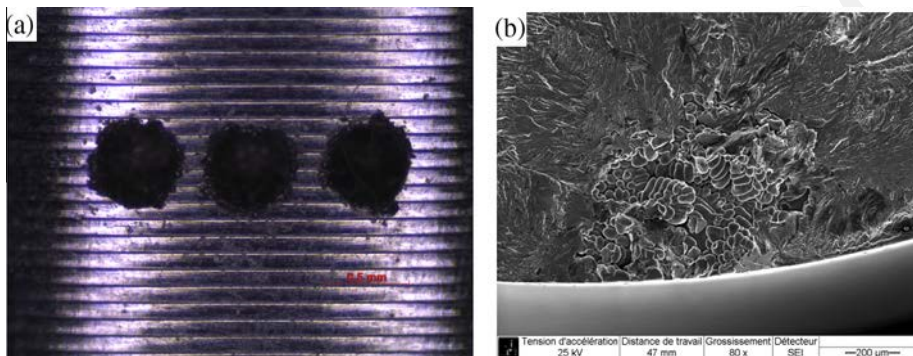


Fig. 13. Competition between shrinkage cavity and 3 artificial defects under fatigue tension.

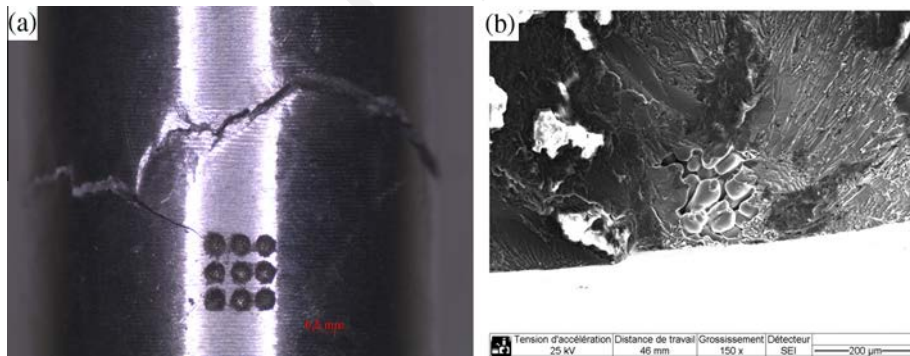


Fig. 14. (a) Specimen surface and (b) fracture surface of a tension–torsion specimen with 9 defects.

4.4. Competition between single and complex defects under both uniaxial and bi-axial loadings

Under uniaxial and multiaxial loadings, there is a competition between single and complex defects. As shown in Fig. 13, 3 artificial defects of a size $\sqrt{area} \approx 400 \mu\text{m}$ are places in a row with a $d_{edge} = 120 \mu\text{m}$. As $d_{edge} < \text{defect size}$, the cumulative size for the complex defect can be calculated using the new criterion proposed in this study. The cumulative \sqrt{area} is equals to $800 \mu\text{m}$. However, the crack which lead to the failure of the specimen was initiated from a shrinkage cavity, whose \sqrt{area} was $706 \mu\text{m}$. This phenomenon can be explained by the Kitagawa diagram. As can be seen from Fig. 8, the defects between 500 and $900 \mu\text{m}$ have similar influence on the fatigue limit. Furthermore, it has been concluded that a natural defect has the same influence on fatigue limit as an artificial defect of the same size. So if several defects coexist in a specimen, there will be competition among them under fatigue loading. Moreover, although not leading to the final failure of specimen, a crack that initiated from 3 defects was found after the test, which proved the viewpoint of defect competition in fatigue, too.

Fig. 14 shows the competition between a shrinkage cavity and artificial defects under tension–torsion. The specimen failed from the shrinkage cavity instead of the artificial defects. The shrinkage had a size in terms of \sqrt{area} of 187 μm , which is smaller than that of a single artificial defect. As in the case under tension, this result can also be explained by Kitagawa diagram. As shown in Fig. 10, σ_D is not influenced by defects smaller than 900 μm in tension–torsion tests. So a specimen can fail from any defect smaller than 900 μm under tension–torsion. As the case in tension, a crack not leading to failure can be found from the artificial defects, as shown in Fig. 14a.

5. Conclusions

Tension, torsion and tension–torsion fatigue tests with load ratios $R = -1$ and 0.1 have been performed on AS7G06-T6 alloy. The “step loading” procedure was used to evaluate the fatigue limit. Both defect-free specimens and those with natural or artificial defects (size between 187 and 860 μm , single or complex defects) have been tested. The Basquin’s law is used to moderate the $S-N$ curves. Crossland criterion and principal stress criterion considering Goodman idea have been tested for multiaxial loadings. A new definition of equivalent defect size for complex defect under fatigue tension is proposed.

- Crossland criterion gives reasonable results in tension, torsion and tension–torsion for two load ratios $R = -1$ and 0.1. The average value of the absolute errors for 5 load types is 7%. The principal stress criterion considering Goodman idea gives less accurate results: the average absolute error for 5 load types is 15%.
- A criterion is proposed in this study to calculate the equivalent defect size for 3 defects:
 - If $d_{edge} < \sqrt{area}$ of one defect, the 3 defects are considered as a big defect and the ligament can be considered in the calculation of the size of the big defect.
 - If $d_{edge} \geq \sqrt{area}$ of one defect, the 3 defects are considered as 3 isolated defects.
- Using the parameter \sqrt{area} to characterize the defect size, a shrinkage cavity has similar influence on the fatigue limit as a spark erosion machining defect of the same size.
- The fatigue limit is not influenced by defects smaller than 900 μm in tension–torsion tests ($\sigma_{a,11} = \sigma_{a,12}$), with a load ratio $R = 0.1$ for AS7G06-T6.
- There is a competition between single and complex defects under both uniaxial and bi-axial loadings. In some cases, a specimen can fail from a small natural shrinkage cavity instead of from big complex artificial defects. Although cracks also initiated from complex defects, they did not lead to the failure of specimen.

More tension–torsion fatigue tests need to be performed to estimate the Crossland criterion. The new criterion to calculate the equivalent size for 3 defects in tension should be confirmed using finite element method. The competition between single and complex defects should be studied in a microscopic scale.

Acknowledgements

This work is part of the IDEFFAAR (Influence des DEFauts de Fonderie sur la Fatigue des Alliages Aéronautiques) project, which is financed by ANR (National Research Agency, through Grant ANR-2010-RMNP-016-01).

References

- [1] Wang YY, Yao WX. Evaluation and comparison of several multiaxial fatigue criteria. *Int J Fatigue* 2004;26:17–25.
- [2] Crossland B. Effect of large hydrostatic pressures on the torsional fatigue strength of fan alloy steel. In: *Proceedings of the international conference on fatigue of metals*, London and New York; 1956. p. 138–49.
- [3] Murakami Y, Endo M. Effects of defects, inclusions and inhomogeneities on fatigue strength. *Int J Fatigue* 1994;16:163–82.
- [4] Murakami Y. Stress concentration. In: Murakami Y, editor. *Metal fatigue: effects of small defects and nonmetallic inclusions*. Oxford: Elsevier; 2002. p. 11–24.
- [5] BS 7910. Guidance on methods for assessing the acceptability of flaws in metallic structures. London, UK: British Standard Institution; 1999 [chapter 7].
- [6] R6. Assessment of the integrity of structures containing defects. Gloucester: British Energy Generation Ltd.; 2001 (revision 4, chapters I and II.3).
- [7] ASME Boiler and pressure vessel design code. Section XI. Philadelphia: American Society of Mechanical Engineers; 1992.
- [8] Twaddle BR, Hancock JW. The development of cracks by defect coalescence. *Fatigue of offshore structures*. EMAS, 1986.
- [9] Iida K, Ando K, Hirata T. An evaluation technique for fatigue life of multiple surface cracks. *Naval Arch Ocean Engng* 1984;22:177–99.
- [10] Leek TH, Howard IC. An examination of methods of assessing interacting surface cracks by comparison with experimental data. *Int J Pressure Vessels Piping* 1996;68:181–201.
- [11] Soboyejo WO, Knott JF, Walsh MJ, Cropper KR. Fatigue crack propagation of coplanar semi-elliptical cracks in pure bending. *Engng Fract Mech* 1990;37:323–40.
- [12] O’Donoghue PE, Nishioka T, Atluri SN. Multiple surface cracks in pressure vessels. *Engng Fract Mech* 1984;20:545–60.
- [13] Perl M, Levy C, Wang J. Interaction effects in combined arrays of radial and longitudinal semi-elliptical surface cracks in pressurised thick-walled cylinder. *J Pressure Vessel Technol Trans ASME* 1997;119:167–73.
- [14] Hasegawa K, Miyazaki K, Kanno S. Interaction criteria for multiple flaws on the basis of stress intensity factors. In: *Proc Int Conf ASME pressure vessels and piping 2001*, Atlanta, Ga. 22–26 July 2001.
- [15] Miller KJ. The behaviour of short fatigue cracks and their initiation Part I—a review of two recent books. *Fatigue Fract Engng Mater Struct* 1987;10:75–91.
- [16] Miller KJ. The behaviour of short fatigue cracks and their initiation Part II—a general summary. *Fatigue Fract Engng Mater Struct* 1987;10:93–113.
- [17] ASTM International, E155-05: Standard Reference Radiographs for Inspection of Aluminum and Magnesium Castings. West Conshohocken; 2005.

- [18] Kitagawa H, Takahashi S. Applicability of fracture mechanics to very small cracks or the cracks in the early stages. In: Proceedings of the second international conference on mechanical behavior of materials, Boston; 1976. p. 627–31.
- [19] Bellows RS, Muju S, Nicholas T. Validation of the step test method for generating Haigh diagrams for Ti–6Al–4V. *Int J Fatigue* 1999;21:687–97.
- [20] Murakami Y, Tazunoki Y, Endo T. Existence of the coxing effect and effects of small artificial holes on fatigue strength of an aluminum alloy and 70–30 brass. *Metall Mater Trans A* 1984;15:2029–38.
- [21] Yi JZ, Gao YX, Lee PD, Flower HM, Lindley TC. Scatter in fatigue life due to effects of porosity in cast A356-T6 aluminum–silicon alloys. *Metall Mater Trans A* 2003;34:1879–90.
- [22] Jana S, Mishra RS, Baumann JB, Grant G. Effect of friction stir processing on fatigue behavior of an investment cast Al–7Si–0.6 Mg alloy. *Acta Mater* 2010;58:989–1003.
- [23] Buffière J-Y, Savelli S, Jouneau PH, Maire E, Fougères R. Experimental study of porosity and its relation to fatigue mechanisms of model Al–Si7–Mg0.3 cast Al alloys. *Mater Sci Engng A* 2001;316:115–26.
- [24] Wang QG, Apelian D, Lados DA. Fatigue behavior of A356-T6 aluminum cast alloys. Part I. effect of casting defects. *J Light Met* 2001;1:73–84.
- [25] Brochu M, Verreman Y, Ajersch F, Bouchard D. High cycle fatigue strength of permanent mold and rheocast aluminum 357 alloy. *Int J Fatigue* 2010;32:1233–42.
- [26] Brochu M, Verreman Y, Ajersch F, Bouchard D. Propagation of short fatigue cracks in permanent and semi-solid mold 357 aluminum alloy. *Int J Fatigue* 2012;36:120–9.
- [27] Koutiri I, Bellett D, Morel F, Augustins L, Adrien J. High cycle fatigue damage mechanisms in cast aluminium subject to complex loads. *Int J Fatigue* 2013;47:44–57.
- [28] Koutiri I, Bellett D, Morel F, Pessard E. A probabilistic model for the high cycle fatigue behaviour of cast aluminium alloys subject to complex loads. *Int J Fatigue* 2013;47:137–47.
- [29] Ben Sghaier R, Bouraoui Ch, Fathallah R, Hassine T, Dogui A. Probabilistic high cycle fatigue behaviour prediction based on global approach criteria. *Int J Fatigue* 2007;29:209–21.
- [30] Internal report of the IDEFFAAR project.
- [31] Yi JZ, Gao YX, Lee PD, Flower HM, Lindley TC. Scatter in fatigue life due to effects of porosity in cast A356-T6 aluminum–silicon alloys. *Mater Trans A* 2003;34:1879–90.
- [32] Luo Z, Zhong E. Derivation of formula for any polygonal area and its applications. *College Math* 2005;21:123–5.
- [33] Roy MJ, Nadot Y, Maijer DM, Benoit G. Multiaxial fatigue behaviour of A356-T6. *Fatigue Fract Engng Mater Struct* 2012;35:1148–59.
- [34] Roy MJ, Nadot Y, Nadot-Martin C, Bardin PG, Maijer DM. Multiaxial Kitagawa analysis of A356-T6. *Int J Fatigue* 2011;33:823–32.